

Research Paper

Complementary autophagy inhibition and glucose metabolism with rattle-structured polydopamine@mesoporous silica nanoparticles for augmented low-temperature photothermal therapy and *in vivo* photoacoustic imaging

Leihou Shao^{1,3*}, Yunhao Li^{2*}, Feifei Huang⁴, Xuan Wang^{1,5}, Jianqing Lu¹, Fan Jia^{1,5}, Zian Pan^{1,5}, Xinyue Cui¹, Guanglu Ge^{1,5}, Xiongwei Deng^{1✉}, and Yan Wu^{1,5✉}

1. CAS Key Laboratory for Biomedical Effects of Nanomaterials and Nanosafety, CAS Key Laboratory of Standardization and Measurement for Nanotechnology, CAS Center for Excellence in Nanoscience, National Center for Nanoscience and Technology, Beijing 100190, P. R. China.
2. Department of General Surgery, Peking Union Medical College Hospital, Peking Union Medical College, Chinese Academy of Medical Sciences, Beijing 100730, P. R. China.
3. Beijing Key Laboratory of Organic Materials Testing Technology and Quality Evaluation, Beijing Center for Physical and Chemical Analysis, Beijing, 100089, China.
4. The Key Laboratory of Beijing City on Preparation and Processing of Novel Polymer Materials, Beijing University of Chemical Technology, Beijing, 100029, China.
5. University of Chinese Academy of Sciences, Beijing 100049, P. R. China.

*These authors contributed equally to this work.

✉ Corresponding authors: E-mails: dengxw2018@nanoctr.cn (X. Deng); wuy@nanoctr.cn (Y. Wu).

© The author(s). This is an open access article distributed under the terms of the Creative Commons Attribution License (<https://creativecommons.org/licenses/by/4.0/>). See <http://ivyspring.com/terms> for full terms and conditions.

Received: 2020.02.07; Accepted: 2020.05.20; Published: 2020.06.05

Abstract

Rattle-structured nanoparticles with movable cores, porous shells and hollow interiors have shown great effectiveness in drug delivery and cancer theranostics. Targeting autophagy and glucose have provided alternative strategies for cancer intervention therapy. Herein, rattle-structured polydopamine@mesoporous silica nanoparticles were prepared for *in vivo* photoacoustic (PA) imaging and augmented low-temperature photothermal therapy (PTT) via complementary autophagy inhibition and glucose metabolism.

Methods: The multifunctional rattle-structured nanoparticles were designed with the nanocore of PDA and the nanoshell of hollow mesoporous silica (PDA@hm) via a four-step process. PDA@hm was then loaded with autophagy inhibitor chloroquine (CQ) and conjugated with glucose consumer glucose oxidase (GOx) (PDA@hm@CQ@GOx), forming a corona-like structure nanoparticle.

Results: The CQ and GOx were loaded into the cavity and decorated onto the surface of PDA@hm, respectively. The GOx-mediated tumor starvation strategy would directly suppress the expression of HSP70 and HSP90, resulting in an enhanced low-temperature PTT induced by PDA nanocore. In addition, autophagy inhibition by the released CQ made up for the loss of low-temperature PTT and starvation efficiencies by PTT- and starvation-activated autophagy, realizing augmented therapy efficacy. Furthermore, the PDA nanocore in the PDA@hm@CQ@GOx could be also used for PA imaging.

Conclusion: Such a “drugs” loaded rattle-structured nanoparticle could be used for augmented low-temperature PTT through complementarily regulating glucose metabolism and inhibiting autophagy and *in vivo* photoacoustic imaging.

Key words: autophagy inhibition, rattle structure, polydopamine, glucose oxidase, low-temperature PTT

Introduction

Photothermal therapy (PTT) has been extensively explored as a potent non-invasive strategy for cancer treatment, which utilizes light-absorbing materials to convert photoenergy into local hyperthermia to ablate tumor tissues [1,2]. However, common PTT strategy generally needs sufficient heating to attain harsh photothermal temperatures (e.g. > 50 °C) to induce effective cell necrosis, which inevitably requires large amount of photothermal agents or a high-power laser density [3-5]. Furthermore, it may also lead to collateral damage to nearby normal tissues and induce inflammatory diseases by the indiscriminate heating. Recently, one emerging strategy to over these limitations could be achieved by mild low-temperature PTT pattern (e.g. < 45 °C). However, the efficacy of low-temperature PTT is restricted and can be repaired by cells themselves through the help of thermal resistance [6-10]. The thermal resistance is mainly ascribed to the effects of heat shock proteins (HSPs), which would also lead to tumor recurrence and metastasis [11-13]. Therefore, it is a feasible strategy to enhance low-temperature PTT by inhibiting the expression of HSPs. Current reversible strategies for thermal resistance were mainly adopted by introducing various HSP inhibitors, including small molecule inhibitors and small interference RNAs [14-15]. Nevertheless, the therapeutic effect by single low-temperature PTT was still restrictive. Therefore, it remains the imperative needs to develop innovate strategy to improve the low-temperature PTT effects.

Cancer starvation therapy is an emerging approach by cutting off the nutrient supply to suppress tumor growth, which is usually achieved via vascular embolization [16-18]. Alternatively, in consideration of the sensitivity of tumor cell to glucose, tumor starvation therapy has drawn great interest by consuming the glucose via biocatalysts [19-21]. In particular, glucose oxidase (GOx) was the most usually used biocatalyst for tumor glucose-metabolism regulation, which could convert glucose to glucose acid and toxic H₂O₂. Specially, the enhanced glucose depletion by GOx would inhibit the ATP production and the expression of HSPs, which would also lead to enhanced PTT effects [9].

Autophagy is a catabolic process maintaining cellular homeostasis through degradation misfolded proteins or damaged organelles by the lysosomal system [22]. In normal tissue, autophagy is a highly conservative cellular process, while dysfunctional autophagy acts a crucial role in many diseases, including cancer, microbial infection and neurodegeneration [23,24]. Moreover, autophagy is

essential for cell survival in response to various cellular stresses. Both metabolic stress and PTT would cause autophagy activation in cancer cells. In addition, emerging studies have revealed that activated autophagy plays an important role in producing resistance against multiple therapeutic approaches [25-29]. Thus, combined autophagy inhibition has been regarded as a prevailing route to enlarge the tumor treatment sensitivity, including chemotherapy, radiation or hyperthermal [30,31].

Owing to their outstanding properties, rattle-type nanostructures with movable cores, porous shells, and interstitial hollow spaces in between, have attracted increasing attention in the fields of nanomedicine [32,33]. Moreover, the nanoparticles could also be an intelligent platform for multispect application by bringing in a multifunctional core. As a neurotransmitter, dopamine was widely distributed in humans [34]. Specially, dopamine could self-polymerize to form surface-adherent polydopamine (PDA) nanoparticles or PDA coatings onto a wide range of inorganic materials [35-38]. Interestingly, the photothermal effect of PDA nanoparticles has also been widely explored for photoacoustic (PA) imaging and PTT with good biocompatibility and photothermal stability [39].

Inspired by these concerns, a multifunctional rattle-structured nanoparticle was designed with the core of PDA and the shell of hollow mesoporous silica (PDA@hm). The central cavity of PDA@hm could be used to load autophagy inhibitor drug chloroquine (CQ) (PDA@hm@CQ). CQ is the only FDA-approved small molecule autophagy inhibitor available for clinical use [40]. The glucose consumer of glucose oxidase (GOx) was concurrently conjugated onto the surface of mesoporous silica shell, forming a corona-like structure (PDA@hm@CQ@GOx) (**Figure 1A**). Thus, a strategy of low-temperature PTT in combination with cell energy metabolism and autophagy inhibition was synchronously proposed in this system (**Figure 1B**). Self-polymerized PDA nanocore from dopamine monomer was utilized as the photothermal conversion agent for low-temperature PTT and photoacoustic (PA) imaging contrast for tumor PA imaging *in vivo*. After entering into cancer cells, the enhanced glucose depletion by GOx could suppress the expression of HSP70 and HSP90, leading to an enhanced low-temperature PTT effect. In addition, inhibition of autophagy by CQ could further enhance the therapeutic effects significantly both *in vitro* and *in vivo* with negligible toxicity. In short, we demonstrated the use of these rattle-structured PDA@hm@CQ@GOx nanoparticles for augmented low-temperature PTT through

synchronously regulating glucose metabolism and inhibiting autophagy with tumor PA imaging ability.

Materials and Methods

Materials

Dopamine hydrochloride was purchased from J&K Chemical Ltd (Beijing, China). Chloroquine diphosphate was purchased from TCI chemical industry development Co., Ltd (Shanghai, China). CCK-8 kit and indocyanine green (ICG) was

purchased from Dojindo Molecular Technologies (Tokyo, Japan). LysoTracker Green was obtained from Molecular Probes Inc. (Eugene, OR). Antibodies were purchased from Abcam, Inc. All other chemicals and solvents were of analytical grade commercially available unless specially mentioned otherwise. Ultrapure water (deionized (DI) water) was supplied by a Milli-Q water system (Millipore, Bedford, MA, USA).

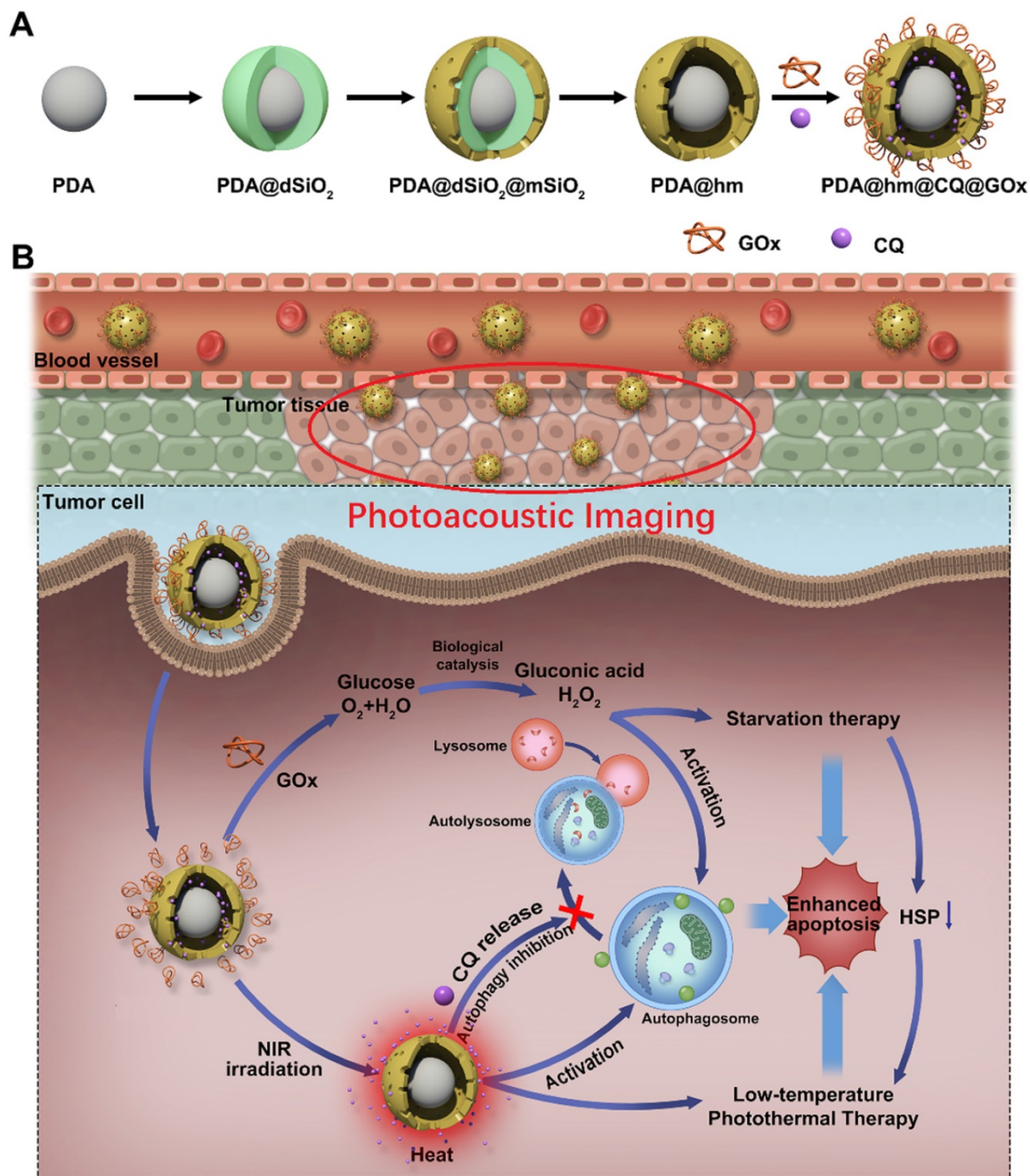


Figure 1. (A) Schematic illustration of the multi-step preparation process of the rattle-structured PDA@hm@CQ@GOx nanoparticles. Polydopamine core/hollow mesoporous silica shell nanoparticles (PDA@hm) with a rattle structure was designed and prepared. CQ was introduced to the large cavity of PDA@hm and GOx was decorated onto the surface of PDA@hm by covalent linkage (PDA@hm@CQ@GOx). (B) Application of the PDA@hm@CQ@GOx for enhanced low-temperature PTT against cancers under NIR laser irradiation by synchronous autophagy inhibition and energy metabolism.

Preparation of PDA, PDA@dSiO₂, PDA@dSiO₂@mSiO₂ and PDA@hm

The PDA nanoparticles were synthesized according to the reported methods [36]. Briefly, 1.2 mL of ammonia aqueous solution was added to a 200 mL of flask containing 45 mL of deionized water and 20 mL of ethanol. The mixed solution was then stirred for 30 min at 30 °C. Then, 250 mg of dopamine hydrochloride dissolved in 5 mL of deionized water was quickly added into the above solution under vigorous stirring and aerobic conditions. After stirring for 24 h, the PDA nanoparticles were obtained by centrifugation and purified by repeated washing with deionized water.

For the synthesis of PDA@dSiO₂, 2 mL of PDA nanoparticles solution (3 mg/mL) was mixed with 0.628 mL of ammonia aqueous solution and 14.28 mL of ethanol in a 50 mL flask under vigorous stirring at 30 °C for 30 min. Then, 0.106 mL of tetraethyl orthosilicate (TEOS) dissolved in 0.94 mL of ethanol was added dropwise into the above solution. After stirring for 30 min at 30 °C, the PDA@dSiO₂ nanoparticles were obtained by centrifugation and purified by repeated washing with ethanol.

Hexadecyl trimethyl ammonium bromide (CTAB) was used as the template to modify PDA@dSiO₂ with mSiO₂ according to the previous work with some modification [41,42]. Typically, 18 mL of deionized water was mixed with 0.8 mL of CTAB (0.2 M) solution and 0.2 mL of NaOH (0.1 M) solution under stirring. 1 mL PDA@dSiO₂ solution was added into the above mixture and stirred for 30 min at 30 °C. Subsequently, 25 µL of TEOS in 225 µL of ethanol was added dropwise into the above solution. After stirring for 30 min at 30 °C, the CTAB molecules were removed by repeated washing with methanol. Finally, the PDA@dSiO₂@mSiO₂ nanoparticles were collected by centrifugation and purified by repeated washing with ethanol, deionized water.

Finally, the intermediate dSiO₂ layer was selectively etched via a typical “surface-protected selective etching” method [42]. 10 mL of PDA@dSiO₂@mSiO₂ solution was mixed with 10 mL of polyvinylpyrrolidone (PVP, Mw=40000) solution and the mixed solution was stirred for 30 min at 30 °C. Then, the temperature was raised to 95 °C and maintained for 2.5 h to etch the layer of dSiO₂. Thereafter, the solution was cooled down to room temperature. The PDA@hm nanoparticles were collected by centrifugation and purified by repeated washing with ethanol and deionized water, respectively.

Preparation of PDA@hm@CQ@GOx

The CQ was loaded on the hollow cavity of PDA@hm. CQ was suspended in deionized water and then added into PDA@hm solution under stirring in the dark at room temperature. After 36 h, the PDA@hm@CQ products were collected via centrifugation and washed with deionized water three times to remove the unloaded CQ. To make GOx covalently grafted onto the surface of PDA@hm, the PDA@hm nanoparticles were treated with 3-aminopropyltrimethoxysilane (APTES) to form the amino groups on their surface. Then, a certain amount of GOx and EDC, NHS were dissolved in 6 mL ultrapure water and stirred for 8 h at room temperature. The amino-functionalized PDA@hm was added into the above solution and further stirred for 24 h. The final PDA@hm@GOx were collected by centrifugation and purified by ultrapure water washing.

Characterizations

Morphological characterizations were conducted by using scanning electron microscopy (SEM) (Hitachi S4800) and transmission electron microscopy (TEM) (Tecnai G2 20 S-TWIN, FEI). Size distribution of nanoparticles was recorded by using a Zeta-sizer NanoZS (Malvern, UK). Nitrogen adsorption-desorption isotherms and pore size distribution curves were measured using Micromeritics Tristar II 3020.

Photothermal evaluation

The photothermal effects of PDA@hm solutions with various concentrations were evaluated by irradiating with an 808 laser at a power density of 1.5 W/cm². The temperature changes were monitored and recorded by an infrared thermal camera.

Cellular uptake assays

To investigate the cellular uptake behavior of the PDA@hm, fluorescent dye ICG was loaded on the hollow cavity of PDA@hm to track the distribution of nanoparticles in cells. HepG-2 cells were seeded in glass-bottomed dishes for 24 h at 37 °C incubator with 5% CO₂. Then, the original culture medium was replaced with the medium containing ICG loaded PDA@hm nanoparticles. After another 0.5, 2, or 4 h incubation, the cells were washed with PBS and then the cell nucleus and lysosomes were stained by Hoechst 33342 and LysoTracker Green, respectively. Finally, the cells uptake images were observed by a confocal laser scan microscopy (CLSM, Carl Zeiss).

Western-blot assays

HepG-2 cells were seeded in a 6-well plate at a density of 1 × 10⁵ cells per well for 24 h and then

performed with different operations. After that, the cells in each group were collected and lysed. The proteins were separated on gel and subsequently transferred onto a poly (vinylidene difluoride) (PVDF) membrane. After blocking with 5% (w/v) milk, the membranes were incubated with the primary antibody overnight at 4 °C and then incubated with the secondary antibody for 1 h at room temperature. A ChemiDoc XR + UV illuminator was used to detect the different protein bands.

In vitro cytotoxicity assays

The *in vitro* cytotoxicity assay was carried out by cell counting kit-8 (CCK-8) assay. HepG-2 cells were cultured in 96-well plates with a density of 5×10^3 cells per well and cultured overnight. After that, the original culture medium was removed and replaced by fresh medium containing various formulations combined with different NIR treatments. After further incubation for 24 h or 48 h, the cells viabilities were measured by CCK-8 assay.

Apoptosis assay by flow cytometry

Flow cytometry assay was used to evaluate the cells apoptosis rate after different formulations treatments. HepG-2 cells were seeded into 6-well plates and cultured overnight. After treated with PBS, PDA@hm, CQ, GOx, PDA@hm+NIR, PDA@hm@CQ+NIR, PDA@hm@GOx+NIR, PDA@hm@CQ@GOx+NIR, the cells in each well were collected and stained with annexin V-FITC and PI, and then detected by flow cytometry.

Autophagy inhibition analysis by TEM

HepG-2 cells were incubated with PDA@hm, CQ, GOx, PDA@hm+NIR, PDA@hm@CQ+NIR, PDA@hm@GOx+NIR, and PDA@hm@CQ@GOx+NIR in culture medium, respectively. After that, the cells were harvested and fixed with 2.5% glutaraldehyde in PBS buffer overnight. After washing, the cells were fixed with 1% osmium and dehydrated with a graded series of ethanol. Subsequently, the cells were embedded in epoxy resin and sectioned (70 nm), stained and finally observed under TEM.

Animals

The animal experiments were conducted following protocols approved by the Experimental Ethics Committee in Beijing. The HepG-2 tumor-bearing mice was generated by the standard subcutaneous inoculation on female BALB/c mice.

In vivo PA imaging

When the tumor volume reached around 150 mm³, the mice were intravenously injected with 100 μL of solution containing PDA@hm@CQ@GOx. The

in vivo imaging was then carried out by a multispectral optoacoustic tomography scanner (MSOT, iThera Medical) at different time points after injection.

In vivo anti-tumor studies

When the tumor volume reached around 100 mm³, the HepG-2 tumor bearing mice were randomly divided into 8 groups (saline, PDA@hm, PDA@hm@CQ, PDA@hm@GOx, PDA@hm+NIR, PDA@hm@CQ+NIR, PDA@hm@GOx+NIR, PDA@hm@CQ@GOx+NIR), and then intravenously administrated with corresponding formulations. After 24 h post-injection, the mice treated with NIR treatment were irradiated by 808 nm NIR laser for 5 min. The tumor volumes of all groups were measured with a digital caliper and calculated by the following formula: tumor volume = tumor width² × tumor length/2. The body weights of mice were also recorded every other day. After 16 days, all the mice were sacrificed and the tumors and main organs were collected for following histological analysis.

Serum biochemical analysis

At the end of treatments, mice were sacrificed and serum were collected for blood biochemical analysis to systemically evaluate the biosafety of various nanoparticles (Charles River Laboratories, Beijing, China).

Statistical analysis

The data were presented as mean ± standard deviation (SD), and the statistical significance was determined on the basis of one-way analysis of variance (ANOVA) followed by two-tailed Student's *t* test. (**P* < 0.05, ***P* < 0.01 and ****P* < 0.001).

Results and Discussion

Synthesis and characterization of PDA@hm@CQ@GOx nanoparticles

The rattle-structured polydopamine core/hollow mesoporous silica shell nanoparticles (PDA@hm) were rationally designed and synthesized by a four-step process depicted in **Figure 1A**. First, PDA nanoparticle was synthesized as the core via self-polymerization of dopamine monomer under alkaline environment with the oxidant of oxygen [36,43]. Second, a dense silica layer was coated onto the surface of PDA nanoparticle to fabricate PDA@dSiO₂ through the hydrolysis of tetraethyl orthosilicate (TEOS). Third, a mesoporous silica shell was further decorated onto the PDA@dSiO₂ by using hexadecyltrimethylammonium bromide (CTAB) as the template via the hydrolysis of TEOS, forming PDA@dSiO₂@mSiO₂ nanoparticles [41,42,44]. Finally,

hot water was used as the etchant to selectively etch out the intermediate $d\text{SiO}_2$ layer and polyvinylpyrrolidone (PVP) was chosen as the protecting agent to protect the surface of outer $m\text{SiO}_2$ shell. An internal cavity between the PDA nanocore and outer mesoporous silica shell was formed via a typical “surface-protected selective etching” method [42,45], generating rattle-structured PDA@hm. The scanning electron microscope (SEM), transmission electron microscope (TEM) and dynamic light scattering (DLS) analysis of PDA, PDA@ $d\text{SiO}_2$, PDA@ $d\text{SiO}_2@m\text{SiO}_2$ and PDA@hm nanoparticles were shown in **Figure 2A-D**, respectively. SEM and TEM results revealed that all the obtained nanoparticles exhibited mono-dispersity and spherical shape. A conspicuous increment in the diameters could be observed after $d\text{SiO}_2$ layer and $m\text{SiO}_2$ shell superposition. The mean diameters of PDA nanocore, PDA@ $d\text{SiO}_2$, PDA@ $d\text{SiO}_2@m\text{SiO}_2$ and PDA@hm were calculated to be 151.73 nm, 205.69 nm, 235.24 nm and 234.77 nm from

the DLS analysis, respectively. In particular, a typical inner hollow structure between the PDA nanocore and $m\text{SiO}_2$ shell could be clearly observed from the TEM image of PDA@hm, confirming the successful construction of rattle-structured nanoparticles (**Figure 2E**). The hollow property of PDA@hm could be used to load drugs and the PDA core could be used as photothermal agent for PTT.

The major elements (Si, O, C) displayed in the element mapping images showed that Si and O signals were distributed within the shell and C signal was mainly distributed within the core, also demonstrating the successful formation of PDA core and $m\text{SiO}_2$ shell in PDA@hm (**Figure 2E**). In addition, the nitrogen adsorption-desorption analysis also confirmed the existence of the hollow structure of PDA@hm. As shown in **Figure S1**, the Brunauer-Emmett-Teller (BET) surface area of PDA@hm was measured to be $169.2 \text{ m}^2/\text{g}$, while the parameter of PDA@ $d\text{SiO}_2@m\text{SiO}_2$ was $129.1 \text{ m}^2/\text{g}$. The increased

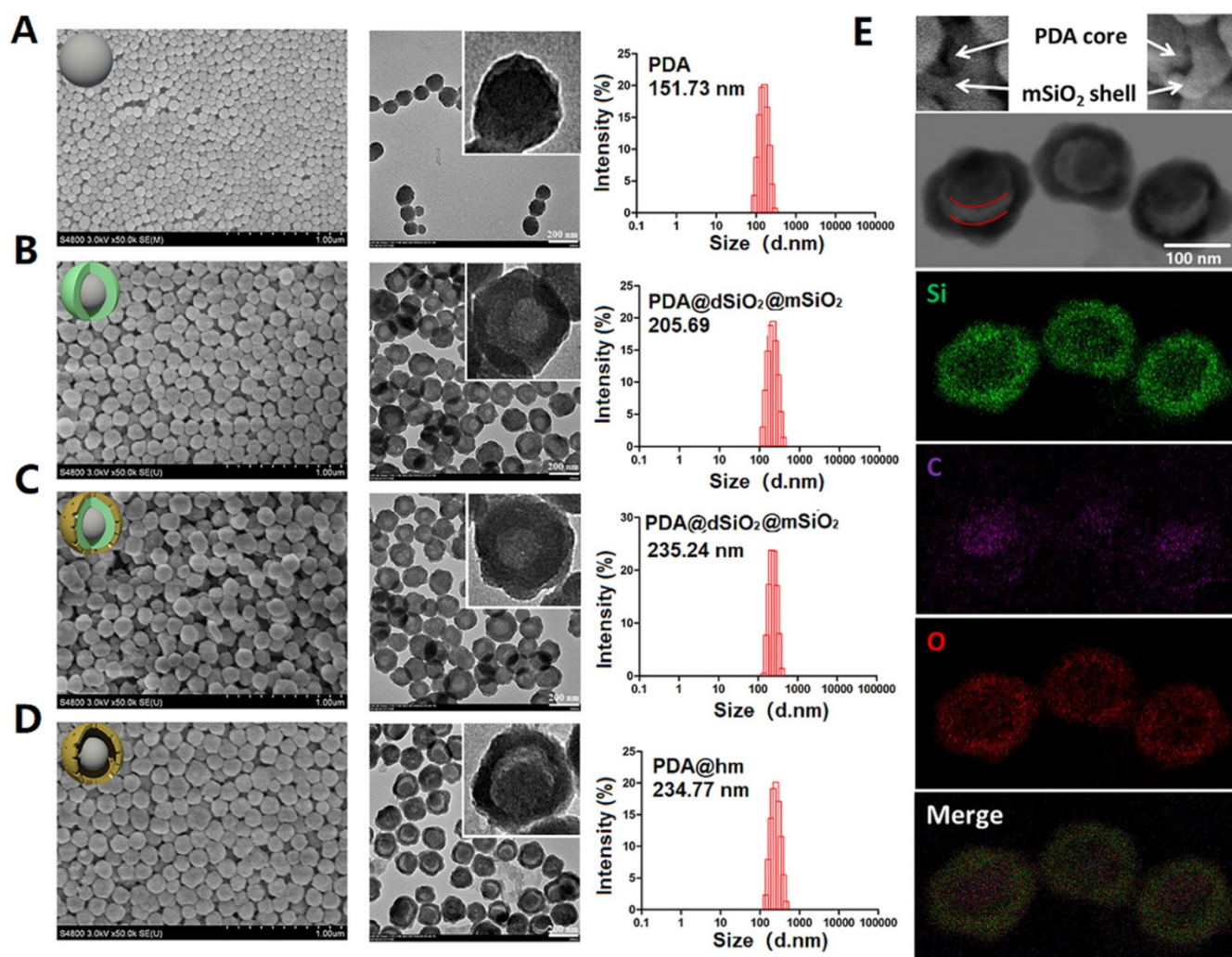


Figure 2. SEM, TEM, DLS and elemental analysis of corresponding nanoparticles. (A) PDA, (B) PDA@dSiO₂, (C) PDA@dSiO₂@mSiO₂, (D) PDA@hm. Average sizes of PDA, PDA@dSiO₂, PDA@dSiO₂@mSiO₂ and PDA@hm were 151.73 nm, 205.69 nm, 235.24 nm and 234.77 nm, respectively. (E) Corresponding elemental (Si, O, C) mappings of PDA@hm.

surface area of PDA@hm could be contributed to the existed hollow cavity in PDA@hm. The average pore diameter of PDA@hm was measured to be 4.9 nm (Figure S2). Subsequently, the autophagy inhibitor CQ was loaded into the hollow cavity and GOx was covalently conjugated onto the surface of PDA@hm, respectively. As calculated, the optimal PDA@hm@CQ was prepared at a mass feeding ratio of 1.5:1 (CQ to PDA@hm) and this ratio was selected in our following experiments. The loading capacity of CQ and the conjugation efficacy of GOx in the obtained PDA@hm@CQ@GOx were 15 wt% and 5 wt%, respectively. DLS, SEM and TEM analysis of PDA@hm@CQ@GOx demonstrated that CQ/GOx incorporation could lead to slight increasement in the size of nanoparticles (Figure S3-S5). Notably, the GOx after conjugation still maintained its high biocatalytic activity to glucose (Figure S6). In addition, the PDA@hm@CQ@GOx exhibited good stability in different solutions after storage in a long time (Figure S7).

Considering that PDA-based nanoparticles could be utilized as photothermal agent to convert NIR light energy to heat [46-49], the photothermal effect of PDA@hm@CQ@GOx was next systematically investigated with an 808 nm laser at a power density of 1.5 W/cm². The photothermal conversion efficiencies of PDA@hm@CQ@GOx at different concentrations (ranging from 25 to 400 µg/mL) were evaluated under 808 nm laser irradiation for 300 s. As shown in Figure 3A, the temperature increasement of PDA@hm@CQ@GOx under laser irradiation exhibited obvious concentration-dependent manner compared with water. When the concentration of PDA@hm@CQ@GOx reached 400 µg/mL, the temperature could increase to 70 °C under continuous irradiation for 300 s whilst the maximal temperature could only increase to about 45 °C with concentration of PDA@hm@CQ@GOx under 100 µg/mL and of 1.5 W/cm² power. In addition, the photothermal conversion efficiency (η) was further measured to assess the photothermal effect of PDA@hm@CQ@GOx (Figure 3B). Based on the cooling curve, the η value of PDA@hm@CQ@GOx was calculated to be 30.4 %, which was similar to the η of PDA nanoparticles. The result suggested that PDA@hm@CQ@GOx exhibited excellent thermal conversion capability (Figure 3C). It also demonstrated that introduction of mSiO₂ shell would not affect the photothermal effects of PDA@hm@CQ@GOx nanoparticles compared with bare PDA nanoparticles.

Having verified the photothermal effect of PDA@hm@CQ@GOx, the photostability of PDA@hm@CQ@GOx was further investigated. As shown in Figure 3D and 3E, the temperature elevation curve

and the peak temperature of PDA@hm@CQ@GOx did not display significant deterioration during the repeated laser exposure treatment, revealing the excellent photothermal stability and reproducibility of PDA@hm@CQ@GOx. In comparison, ICG was easily photobleached and the photothermal effect dropped obviously after five cycles (Figure S8). In addition, TEM and DLS analysis indicated that PDA@hm@CQ@GOx still maintained their morphology and size after 5 irradiation cycles, revealing their high stability (Figure 3F and 3G). Furthermore, the *in vitro* release profiles of CQ from PDA@hm@CQ@GOx indicated that both NIR laser irradiation and mild acidic condition could accelerate CQ release (Figure S9).

***In vitro* therapeutic effects of PDA@hm@CQ@GOx**

For cellular uptake studies, indocyanine green (ICG) was used as a model fluorescence molecule loaded into the PDA@hm@ICG@GOx to evaluate the tumor cell uptake behavior by confocal fluorescence microscopy (CLSM). As shown in Figure 4A, after co-incubation with PDA@hm@ICG@GOx, the ICG signals could be distinguishable in the HepG-2 cells for 0.5 h. As time extended, the signals became more legible, indicating that PDA@hm@ICG@GOx could be efficiently taken up by HepG-2 cells. Meanwhile, most ICG fluorescence overlapped well with the red fluorescence related to lysosome, demonstrating that the nanoparticles may be internalized by cell endocytosis pathway. The biocompatibility of PDA@hm nanoparticles *in vitro* was therefore evaluated by using HepG-2 cells. As shown in Figure 4B, the cell viabilities were still above 90% even at a high concentration of 200 µg/mL, indicating no obvious cytotoxicity was observed in HepG-2 cells after incubation with PDA or PDA@hm nanoparticles for 24 h and 48 h. These results confirmed that the synthesized PDA@hm nanoparticles exhibited good biocompatibility in *in vitro* condition.

We next assessed the therapeutic effects of PDA@hm@CQ@GOx in HepG-2 cancer cells. Herein, we incubated HepG-2 cells with different formulations and then irradiated with 808 nm laser (1.5 W cm⁻², 5 min) to keep the temperature of cell culture around 45 °C. First, Annexin V-fluorescein isothiocyanate (Annexin V-FITC)/propidium iodide (PI) fluorescence staining was carried out to evaluate the apoptotic and necrotic cells after different treatments by flow cytometry assay. As illustrated in Figure 4C, compared with the control, increased cells apoptosis could be observed from the PDA@hm+NIR-, GOx-, and CQ-treated cells, indicating that individual thermal, starvation and autophagy inhibition treatment could induce cell apoptosis. The

PDA@hm@CQ+NIR- and PDA@hm@GOx+NIR-treated cells displayed higher apoptosis ratios (72.06% and 76.58%) as compared to single therapy group, indicating the starvation and autophagy inhibition treatment could enhance the pro-apoptotic effect of low-temperature PTT. The highest cell apoptosis ratio reaching almost ~96% was detected in the cells treated with PDA@hm@CQ@GOx+NIR (**Figure 4D**).

Furthermore, the cytotoxicity of HepG-2 cells treated with different formulations with or without NIR laser exposure was therefore assessed. As shown in **Figure 5A**, the treatment of CQ, GOx, PDA@hm@CQ and PDA@hm@GOx all displayed a moderate killing effect, implying that individual autophagy inhibition by CQ and glucose depletion by GOx could induce cell death to a certain degree. In comparison, CQ+GOx or PDA@hm@CQ@GOx treatment could lead to a higher cell death rate (nearly 50%), indicated

that combining autophagy inhibition and glucose-metabolism regulation resulted in enhanced cells damage effect. PDA@hm upon NIR laser exposure only displayed a moderate killing effect (~75%) due to the limited photothermal effect by low-temperature PTT. By contrast, under equivalent NIR laser exposure, PDA@hm@GOx- or PDA@hm@CQ-treated cells could induce much more cell killing effect than bare CQ or GOx. Of special note, HepG-2 cells treated with PDA@hm@CQ@GOx under NIR laser irradiation displayed the highest cell killing effect nearly 95%. Apoptosis assay together with the cytotoxicity results revealed that mild thermal treatment with synergetic GOx-mediated starvation and CQ-mediated autophagy inhibition by PDA@hm@CQ@GOx+NIR could achieve significant effective PTT performance.

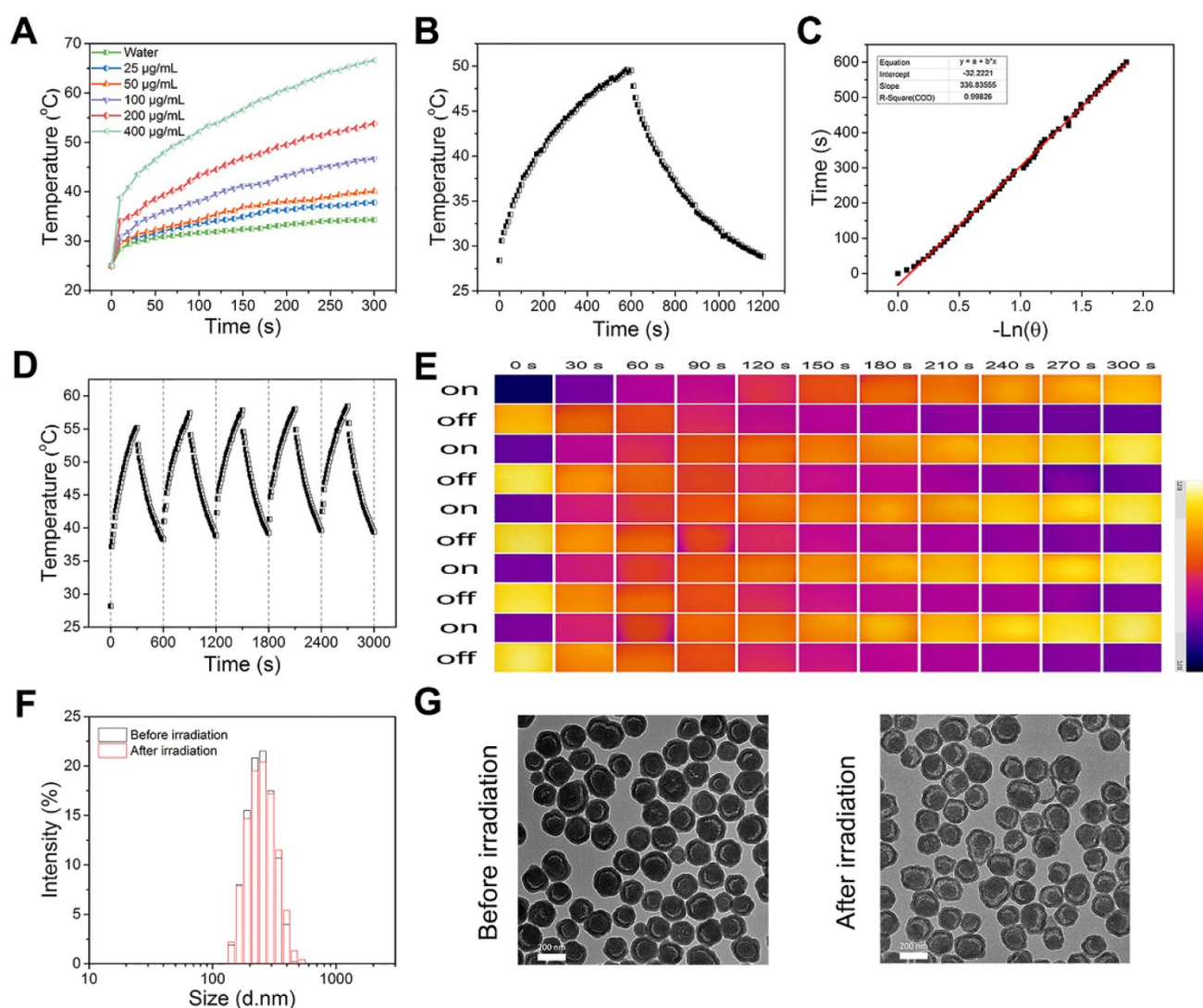


Figure 3. (A) Photothermal-heating curves of PDA@hm@CQ@GOx solutions at different concentrations under 808 nm laser irradiation. (B) Temperature changes of PDA@hm@CQ@GOx solution under 808 nm laser irradiation for 600 s, and then followed by a cooling period. (C) The time constant (τ_c) for the heat transfer in this system calculated from the linear time data during the cooling period. (D) Photothermal stability of PDA@hm@CQ@GOx solution over repeated irradiation on/off cycles. (E) The corresponding thermal images of PDA@hm@CQ@GOx solution over repeated irradiation on/off cycles. (F) Hydrodynamic diameters of the PDA@hm@CQ@GOx before and after 808 nm laser irradiation measured by using DLS. (G) TEM images of the PDA@hm@CQ@GOx before and after 808 nm laser irradiation.

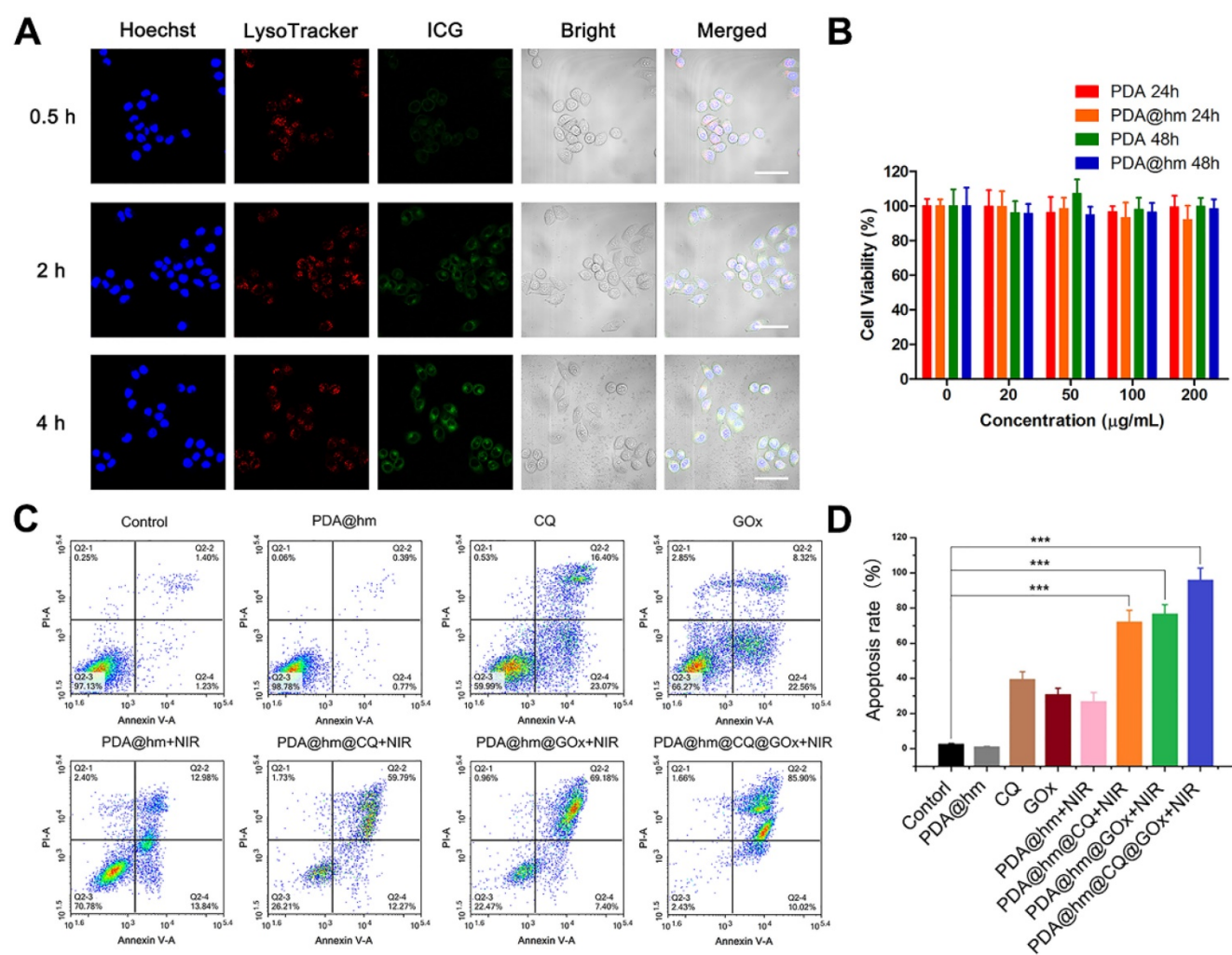


Figure 4. (A) CLSM images of the HepG-2 cancer cells after treatment with PDA@hm@ICG@GOx nanoparticles for 0.5 h, 2 h and 4 h. Cells were stained with Hoechst 33342 and LysoTracker Green, respectively (Scale bar: 50 µm). (B) Relative viabilities of HepG-2 cells after incubation with PDA or PDA@hm nanoparticles for 24 h or 48 h, respectively. (C) Apoptosis rates of HepG-2 cells treated with different formulations determined by flow cytometric analysis. (D) Relative apoptosis rates after different formulations treatments. ****p* < 0.001.

HSPs suppression and autophagy inhibition induced by PDA@hm@CQ@GOx

We next investigated the related mechanisms based on the above cell apoptosis and cytotoxicity results. As documented in the literature, the glucose depletion by GOx could suppress the expression of HSPs [50]. Therefore, the expression of HSP70 and HSP90 in HepG-2 cells after treated with different formulations were investigated by western-blot analysis (Figure 5B). In contrast to the control group, the HSP70 and HSP90 expression were significantly elevated in HepG-2 cells after treated with PDA@hm+NIR, validating that the generation of HSPs could be triggered by increasing the temperature of cancer cells after PTT treatment. However, the expression of HSP70 and HSP90 in cells after thermal treatment could be significantly reduced by PDA@hm@GOx and PDA@hm@CQ@GOx. These results demonstrated that the interference of glucose

metabolism by GOx could effectively suppress the HSPs expression during thermal therapy.

According to previous reports, the induction of autophagy in cancer cells would occur in response to chemotherapy, metabolic stress and thermal treatment [31,51-53]. Hence, targeting autophagy has been recognized as complementary strategy in cancer therapy due to the resistance of autophagy-related tolerance. Next, we investigated the intracellular autophagy situations under different treatments. So far, TEM and western-blot analysis were the most reliable methods to evaluate autophagy level in cells. Therefore, we investigated the autophagy behaviors in cancer cells after different treatments via both western-blot and TEM analysis. During autophagy process, microtubule-associated light chain 3-I (LC3-I) protein is recruited and accumulated on the membrane of the autophagosomes, and subsequently carries out the transition process from LC3 I form into LC3 II form, which is the mark of the autophagosomes

maturation [54]. According to **Figure 5C**, both GOx and PDA@hm+NIR-treated cells displayed increased LC3-II protein level compared with the control cells, confirming the activation of autophagy by starvation and photothermal treatment. CQ-treated cells also exhibited an obvious increased LC3-II protein as it inhibited the degradation of the autophagosomes via disturbing the lysosome activity and thus caused LC3-II protein accumulation within the cytoplasm [55]. Specially, significant increased expression of LC3-II protein could be seen from PDA@hm@CQ@GOx+NIR-treated cells. Furthermore, TEM analysis was utilized to directly observe the autophagy behavior of HepG-2 cells after different treatments. As shown in **Figure 5D**, in consistence with the western-blot results, both GOx and PDA@hm+NIR-treated cells contained more autophagosomes and other autophagic vesicles as compared to the control cells. Due to the inhibition effect of the degradation of autolysosomes, many autophagic vesicles could be clearly observed after CQ treatment. Meanwhile, much more autophagic vesicles could be seen from PDA@hm@CQ@GOx+NIR-treated cells. Altogether, these results strongly confirmed that PDA@hm@CQ@GOx+NIR-treated cells could induce autophagy inhibition in cancer cells, sensitizing the PDA@hm-mediated PTT and GOx-mediated starvation therapeutic effect. With the western-blot results, the outstanding therapy effects of PDA@hm@CQ@GOx+

NIR treatment could simultaneously be attributed to the sensitivity of tumor cells to hyperthermia via GOx-mediated starvation and CQ-mediated autophagy inhibition effect.

In vivo imaging and anti-tumor studies

It has been illustrated that the PDA component could be served as a contrast agent for photoacoustic (PA) imaging. Therefore, the possibility of PDA@hm@CQ@GOx for PA imaging was firstly assessed *in vitro*. As depicted in **Figure 6A** and **6B**, the PA signal heightened with the increasing concentrations of PDA@hm@CQ@GOx and exhibited a linear relationship between the PA signal intensity and concentration. The results demonstrated the potential PA imaging capability of PDA@hm@CQ@GOx. In addition, the blood hemolysis of PDA@hm@CQ@GOx was carried out and the result demonstrated that the favorable blood compatibility of these nanoparticles (**Figure S10**). Subsequently, *in vivo* PA imaging was carried out on HepG-2 tumor-bearing mice after intravenous injection with PDA@hm@CQ@GOx. Remarkably, the PA signals in the tumor site could be clearly distinguished and observed in PDA@hm@CQ@GOx-injected mice after 12 h (**Figure 6C**). Collectively, the *in vitro* and *in vivo* imaging results indicated that the PDA@hm@CQ@GOx nanoparticles could be used for tumor PA imaging to a certain degree.

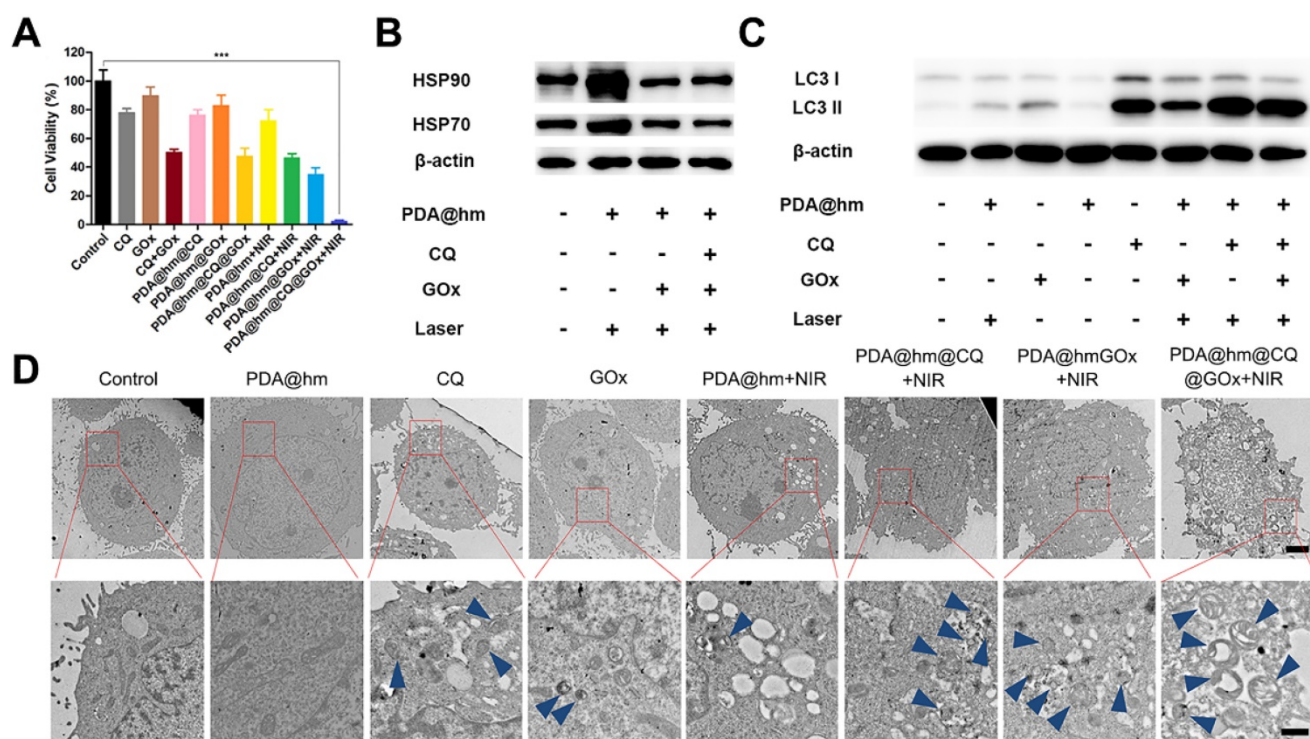


Figure 5. (A) Augmented cell cytotoxicity by mild PTT in combination with glucose consumer GOx and autophagy inhibitor CQ in HepG-2 cells. (B) Representative expression of HSP90 and HSP70 after different treatments by western-blot analysis. (C) Relative LC3-I and LC3-II expression in HepG-2 cells after different treatments. β -actin was used as an internal control. (D) Representative TEM images of HepG-2 cells after different treatments. Blue arrows indicated the autophagosome and autolysosome (Scale bar: 2 μ m in the upper figure and 500 nm in the enlarged figure). *** $p < 0.001$.

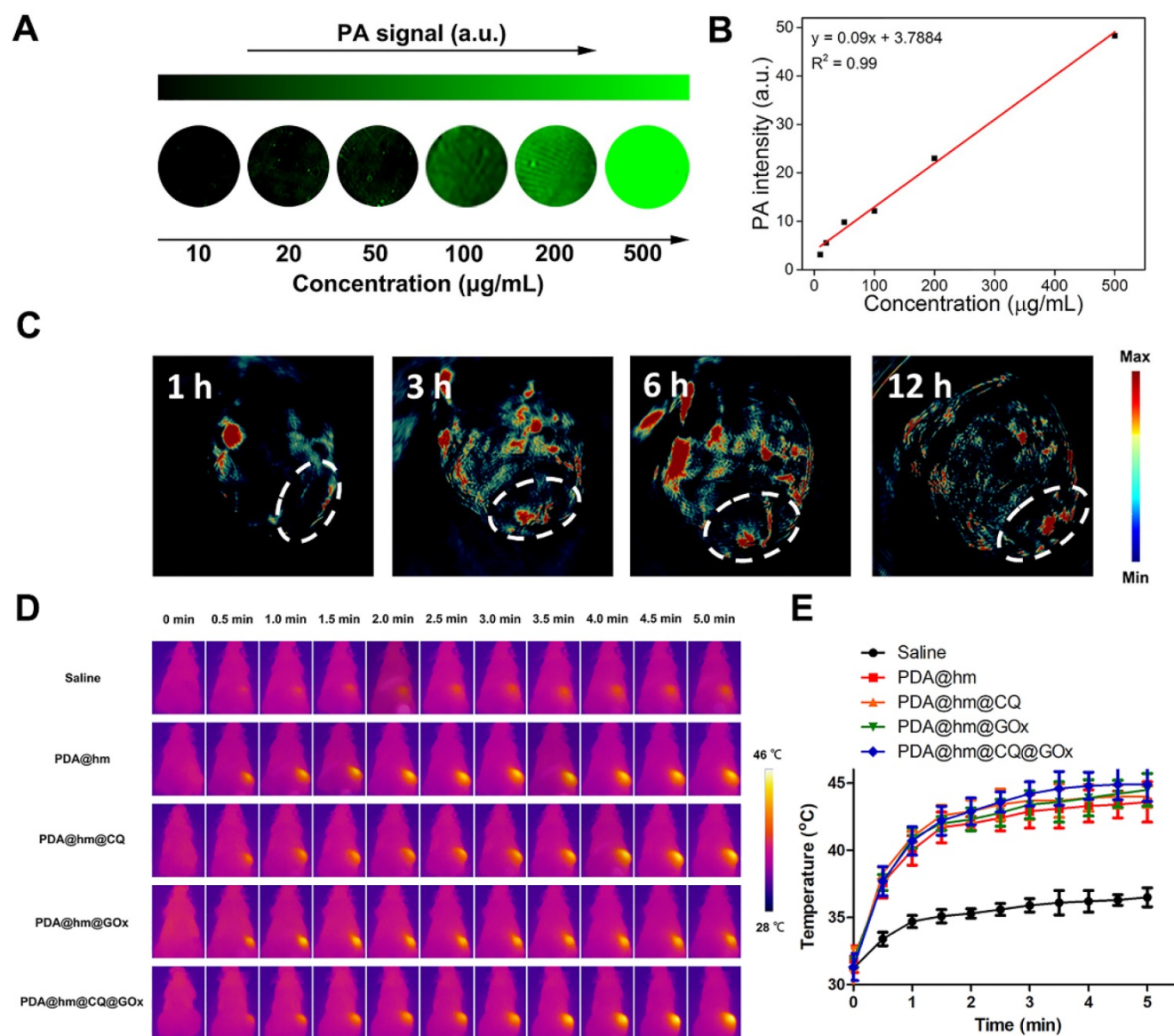


Figure 6. (A) *In vitro* PA imaging of the PDA@hm@CQ@GOx solution at different concentrations. (B) The corresponding quantitative curve of PA intensity at different concentrations. (C) *In vivo* PA images of mice taken at 1 h, 3 h, 6 h and 12 h after i.v. injection of PDA@hm@CQ@GOx. (D) IR thermal images of HepG-2 tumor-bearing mice exposed to 808 nm laser for 5 min. (E) The corresponding temperature changes at the tumor sites.

Encouraged by the *in vitro* synergistic therapeutic results, we then systematically investigated the *in vivo* antitumor effects of different formulations with or without laser treatment in HepG-2 tumor-bearing mice. When the tumor volume reached to $\sim 100 \text{ mm}^3$, the mice were randomly divided into 8 groups and then intravenously injected with saline, PDA@hm, PDA@hm@CQ, PDA@hm@GOx, PDA@hm+NIR, PDA@hm@CQ+NIR, PDA@hm@GOx+NIR and PDA@hm@CQ@GOx+NIR, respectively. An IR thermal camera was used to record the tumor temperature changes under NIR laser irradiation. As illustrated in **Figure 6D** and **6E**, the photothermal heating profile displayed similar temperature increase at the tumor regions in all the PDA-containing nanoparticles-treated groups and

the ultimate tumor temperatures reached to about 45 $^{\circ}\text{C}$. In comparison, the temperature in saline-injected mice only exhibited a slight increase under the same laser irradiation. The tumor volumes were continuously measured and recorded after various treatments and the progressive growth curves of the implanted tumors were summarized in **Figure 7A** and **7B**. It demonstrated that the tumors in saline- and PDA@hm-treated mice grew rapidly. In the absence of NIR laser irradiation, both PDA@hm@GOx- and PDA@hm@CQ-treated mice displayed a moderate inhibition effect in tumor growth, demonstrating that individual GOx- and CQ-incorporated nanoparticles could inhibit tumor growth *in vivo*. PDA@hm+NIR-treated group only showed partially delay on the tumor growth, which could be attributed to that the

low-temperature thermal (about 45 °C) was not enough for effective tumor ablation. Interestingly, the mice treated with PDA@hm@GOx or PDA@hm@CQ under NIR laser irradiation showed higher inhibition effects than any other single treatment on the tumor growth, implying the enhanced therapeutic effects of GOx and CQ supplemented in the low-temperature PTT. Extraordinary tumor regression could be observed in PDA@hm@CQ@GOx+NIR-treated mice and no relapse occurred at the end of the experimental period. The photographs of typical mice received different treatments at 16 days were also recorded (Figure S11). Such a superior antitumor effect resulted from enhanced low-temperature PTT effects through synchronously regulating glucose metabolism and inhibiting autophagy. All mice were euthanized on the 16th day and the tumor tissues from each group were collected and weighted. As shown in Figure 7C, the observed trends of average tumor weights also confirmed that the superior anti-tumor performance of the PDA@hm@CQ@GOx+NIR treatment. These results suggested that low-temperature PTT supplemented with GOx-mediated starvation and CQ-mediated autophagy inhibition could result in more efficient therapeutic effects.

During the therapeutic period, the body weights of mice were also measured and recorded. As shown in Figure S12, no obvious body weight drop was seen from all mice, implying that all treatments had negligible acute systemic toxicity. In addition, various serum biochemistry indexes, including albumin (ALB), alkaline phosphatase (ALP), alanine aminotransferase (ALT), aspartate transaminase (AST), creatine kinase (CK), lactate dehydrogenase (LDH), blood urea nitrogen (BUN), and creatinine (CREA), had no significant changes (Figure 7D). These results also demonstrated the good biocompatibility of PDA@hm@CQ@GOx with or without laser treatment. Moreover, a typical hematoxylin and eosin (H&E) staining method was performed to analyze the corresponding histological changes of the major organs (heart, liver, spleen, lung, kidney) after different treatments. No evident physiological morphology changes were observed in all organs, demonstrating no obvious systemic toxicity of PDA@hm@CQ@GOx (Figure S13). Taken together, the above results demonstrated that PDA@hm@CQ@GOx had a good biocompatibility *in vivo*.

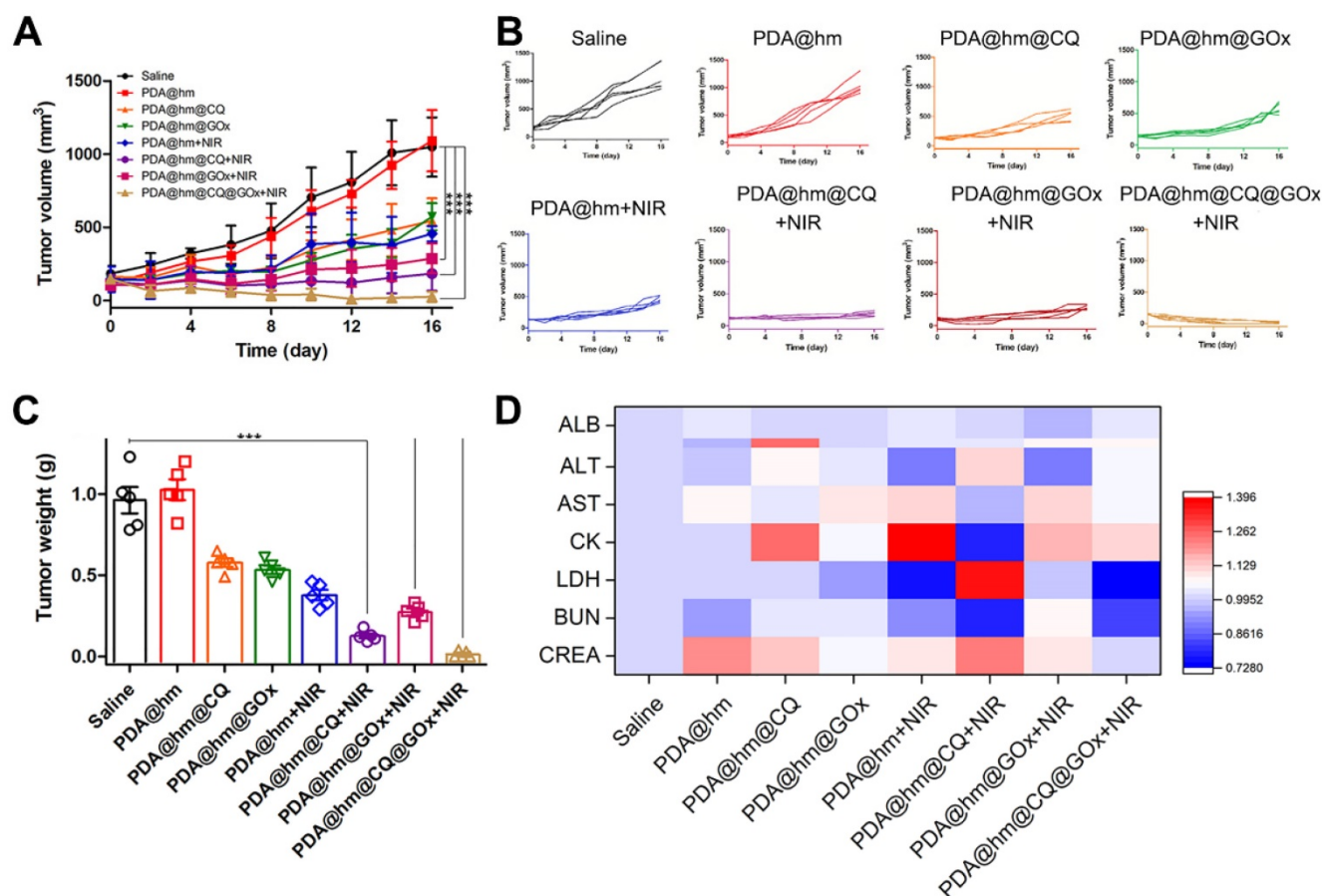


Figure 7. (A) Tumor growth curves of mice after various treatments in 16 days. (B) Individual tumor growth curves of the mice. (C) The average tumor weights after various treatments for 16 days. (D) Blood analysis of mice at 16 days after various treatments with heat map compared with the saline-treated mice. ***p < 0.001 versus the control group.

Conclusions

In conclusion, we successfully developed rattle-structured polydopamine core/hollow mesoporous silica shell nanoparticles (PDA@hm). A strategy of augmented low-temperature PTT in combination with cells autophagy inhibition and energy metabolism regulation was proposed for trimodal complementary cancer therapy. The glucose consumer GOx and autophagy inhibitor CQ were decorated onto the surface and loaded into the cavity of PDA@hm, respectively. The GOx-mediated tumor starvation would directly suppress the expression of HSPs, resulting in an enhanced low-temperature PTT induced by PDA nanocore. Excellently, inhibition of autophagy by the released CQ made up for the loss of low-temperature PTT and starvation efficiencies by PTT- and starvation-activated autophagy, realizing augmented therapeutic efficacy. The improved therapeutic efficacy from the mild thermal combination therapy was confirmed both *in vitro* and *in vivo*. In addition, the PDA@hm@CQ@GOx could be used as a PA contrast agent for PA imaging. Overall, this study provided a proof-of-concept for enhanced mild PTT through regulating glucose metabolism and inhibiting autophagy.

Abbreviations

PA: photoacoustic; PTT: photothermal therapy; GOx: glucose oxidase; PDA: polydopamine; CQ: chloroquine; FDA: Food and Drug Administration; HSP: heat shock protein; PDA@hm: polydopamine core/hollow mesoporous silica shell nanoparticles; CCK-8: cell counting kit-8; ICG: indocyanine green; TEOS: tetraethyl orthosilicate; CTAB: hexadecyl trimethyl ammonium bromide; PVP: polyvinylpyrrolidone; APTES: 3-aminopropyltrimethoxysilane; TEM: transmission electron microscopy; SEM: scanning electron microscopy; DLS: dynamic light scattering; CLSM: confocal laser scan microscopy; PVDF: poly (vinylidene difluoride); MSOT: multispectral optoacoustic tomography scanner; SD: standard deviation; ANOVA: one-way analysis of variance; BET: brunauer-emmett-teller; NIR: near-infrared; FITC: fluorescein isothiocyanate; PI: propidium iodide; LC3: microtubule-associated light chain 3; ALB: albumin; ALP: alkaline phosphatase; ALT: alanine aminotransferase; AST: aspartate transaminase; CK: creatine kinase; LDH: lactate dehydrogenase; BUN: blood urea nitrogen; CREA: creatinine.

Supplementary Material

Supplementary figures.

<http://www.thno.org/v10p7273s1.pdf>

Acknowledgements

This study was supported by the National Key Research and Development Program of China (2016YFA0200902), and supported by National Natural Science Foundation of China (81773185 and 81472850).

Competing Interests

The authors have declared that no competing interest exists.

References

1. Chu K, Dupuy D. Thermal ablation of tumours: biological mechanisms and advances in therapy. *Nat Rev Cancer*. 2014; 14:199-208.
2. Cheng L, Wang C, Feng L, Yang K, Liu Z. Functional nanomaterials for phototherapies of cancer. *Chem Rev*. 2014; 114: 10869-10939.
3. Sun M, Guo J, Hao H, Tong T, Wang K, Gao W. Tumour-homing chimeric polypeptide-conjugated polypyrrole nanoparticles for imaging-guided synergistic photothermal and chemical therapy of cancer. *Theranostics*. 2018; 8: 2634-2645.
4. Liu H, Chen D, Li L, Liu T, Tan L, Wu X, et al. Multifunctional gold nanoshells on silica nanorattles: a platform for the combination of photothermal therapy and chemotherapy with low systemic toxicity. *Angew Chem Int Ed Engl*. 2011; 50: 891-895.
5. Hu D, Zhang J, Gao G, Sheng Z, Cui H, Cai L. Indocyanine green-loaded polydopamine-reduced graphene oxide nanocomposites with amplifying photoacoustic and photothermal effects for cancer theranostics. *Theranostics*. 2016; 6: 1043-1052.
6. Wang B, Yu X, Wang J, Li Z, Li P, Wang H, et al. Gold-nanorods-siRNA nanocomplex for improved photothermal therapy by gene silencing. *Biomaterials*. 2016; 78:27-39.
7. Zhang S, Guo W, Wei J, Li C, Liang X, Yin M. Terrylenediimide-based intrinsic theranostic nanomedicines with high photothermal conversion efficiency for photoacoustic imaging-guided cancer therapy. *ACS Nano*. 2017; 11:3797-3805.
8. Zhu X, Feng W, Chang J, Tan Y, J Li, Chen M, et al. Temperature-feedback upconversion nanocomposite for accurate photothermal therapy at facile temperature. *Nat Commun*. 2016; 7: 10437.
9. Zhou J, Li M, Hou Y, Luo Z, Chen Q, Cao H, et al. Engineering of a nanosized biocatalyst for combined tumor starvation and low-temperature photothermal therapy. *ACS Nano*. 2018; 12: 2858-2872.
10. Yang Y, Zhu W, Dong Z, Chao Y, Xu L, Chen M, et al. 1D coordination polymer nanofibers for low-temperature photothermal therapy. *Adv Mater*. 2017; 29: 1703588.
11. Zhang K, Meng X, Cao Y, Yang Z, Dong H, Zhang Y, et al. Metal-organic framework nanoshuttle for synergistic photodynamic and low-temperature photothermal therapy. *Adv Funct Mater*. 2018; 28:1804634.
12. Zhou Z, Yan Y, Hu K, Zou Y, Li Y, Ma R, et al. Autophagy inhibition enabled efficient photothermal therapy at a mild temperature. *Biomaterials*. 2017; 141: 116-124.
13. Zhang Y, Sha R, Zhang L, Zhang W, Jin P, Xu W, et al. Harnessing copper-palladium alloy tetrapod nanoparticle-induced pro-survival autophagy for optimized photothermal therapy of drug-resistant cancer. *Nat Commun*. 2018; 9: 4236.
14. Chen W, Luo G, Lei Q, Hong S, Qiu W, Liu L, et al. Overcoming the heat endurance of tumor cells by interfering the anaerobic glycolysis metabolism for improved photothermal therapy. *ACS Nano*. 2017; 11: 1419-1431.
15. Tan Y, Zhu Y, Wen L, Yang X, Liu X, Meng T, et al. Mitochondria-responsive drug release along with heat shock mediated by multifunctional glycolipid micelles for precise cancer chemo-phototherapy. *Theranostics*. 2019; 9: 691-707.
16. Jing L, Qu H, Wu D, Zhu C, Yang Y, Jin X, et al. Platelet-camouflaged nanococktail: Simultaneous inhibition of drug-resistant tumor growth and metastasis via a cancer cells and tumor vasculature dual-targeting strategy. *Theranostics*. 2018; 8: 2683-95.
17. Hu J, Liu M, Gao F, Chen Y, Peng S, Li Z, et al. Photo-controlled liquid metal nanoparticle-enzyme for starvation/photothermal therapy of tumor by win-win cooperation. *Biomaterials*. 2019; 217:119303.
18. Yu S, Chen Z, Zeng X, Chen X, Gu Z. Advances in nanomedicine for cancer starvation therapy. *Theranostics*. 2019; 9: 8026-8047.
19. Chen H, Jiang X, Zheng R, Zuo S, Zhao L, Fang G, et al. A biomimetic cascade nanoreactor for tumor targeted starvation therapy-amplified chemotherapy. *Biomaterials*. 2019; 195: 75-85.
20. Lin H, Chen Y, Shi J. Nanoparticle-triggered in situ catalytic chemical reactions for tumour-specific therapy. *Chem Soc Rev*. 2018; 47: 1938-1958.
21. Li S, Cheng H, Xie B, Qiu W, Zeng J, Li C, et al. Cancer cell membrane camouflaged cascade bioreactor for cancer targeted starvation and photodynamic therapy. *ACS Nano*. 2017; 11: 7006-7018.

22. Yang Z, Chee CE, Huang S, Sinicrope FA. The role of autophagy in cancer: therapeutic implications. *Mol Cancer Ther.* 2011; 10: 1533-1541.
23. Zhang X, Yang Y, Liang X, Zeng X, Liu Z, Tao W. Enhancing therapeutic effects of docetaxel-loaded dendritic copolymer nanoparticles by co-treatment with autophagy inhibitor on breast cancer. *Theranostics.* 2014; 4: 1085-1095.
24. Komatsu M, Waguri C, Murata S, Iwata J, Tanida I, et al. Loss of autophagy in the central nervous system causes neurodegeneration in mice. *Nature.* 2006; 441: 880-884.
25. Liang X, De Vera ME, Buchser WJ, Vivar Chavez AR, Loughran P, Stolz DB, et al. Inhibiting systemic autophagy during interleukin 2 immunotherapy promotes long-term tumor regression. *Cancer Res.* 2012; 72: 2791-2801.
26. Li J, Hou N, Faried A, Tsutsumi S, Kuwano H. Inhibition of autophagy augments 5-fluorouracil chemotherapy in human colon cancer in vitro and *in vivo* model. *Eur J Cancer.* 2010; 46: 1900-1909.
27. Chaachouay H, Ohneseit P, Toulany M, Kehlbach R, Multhoff G, Rodemann HP. Autophagy contributes to resistance of tumor cells to ionizing radiation. *Oncol.* 2011; 99: 287-292.
28. Wei M, Chen M, Chen K, Lou P, Lin S, Hung S, et al. Autophagy promotes resistance to photodynamic therapy-induced apoptosis selectively in colorectal cancer stem-like cells. *Autophagy.* 2014; 10: 1179-1192.
29. Zhou Z, Yan Y, Wang L, Chen Y. Melanin-like nanoparticles decorated with an autophagy-inducing peptide for efficient targeted photothermal therapy. *Biomaterials.* 2019; 203: 63-72.
30. Janku F, McConkey DJ, Hong D, Kurzrock R. Autophagy as a target for anticancer therapy. *Nat Rev Clin Oncol.* 2011; 8: 528-539.
31. Chen T, Chen D, Ren Z, Wang Y, Cai X, Huang J, et al. Bismuth embedded silica nanoparticles loaded with autophagy suppressant to promote photothermal therapy. *Biomaterials.* 2019; 221: 119419.
32. Lu S, Tu DT, Hu P, Xu J, Li R, Wang M, et al. Multifunctional nano-bioprobes based on rattle-structured upconverting luminescent nanoparticles. *Angew Chem Int Ed Engl.* 2015; 54: 7915-7919.
33. Chen X, Zhang Q, Li J, Yang M, Zhao N, Xu F. Rattle-structured rough nanocapsules with *in-situ*-formed gold nanorod cores for complementary gene/chemo/photothermal therapy. *ACS Nano.* 2018; 12: 5646-5656.
34. Liu Y, Ai K, Lu L. Polydopamine and its derivative materials: synthesis and promising applications in energy, environmental, and biomedical fields. *Chem Rev.* 2014; 114: 5057-5115.
35. Chen W, Qin M, Chen X, Wang Q, Zhang Z, Sun X. Combining photothermal therapy and immunotherapy against melanoma by polydopamine-coated Al₂O₃ nanoparticles. *Theranostics.* 2018; 8: 2229-2241.
36. Dong Z, Gong H, Gao M, Zhu W, Sun X, Feng L, et al. Polydopamine nanoparticles as a versatile molecular loading platform to enable imaging-guided cancer combination therapy. *Theranostics.* 2016; 6: 1031-1042.
37. Zhong X, Yang K, Dong Z, Yi X, Wang Y, Ge C, et al. Polydopamine as a biocompatible multifunctional nanocarrier for combined radioisotope therapy and chemotherapy of cancer. *Adv Funct Mater.* 2015; 25: 7327-7336.
38. Wang C, Wang D, Dai T, Xu P, Wu P, Zou Y, et al. Skin pigmentation-inspired polydopamine sunscreens. *Adv Funct Mater.* 2018; 28: 1802127.
39. Wang Y, Song S, Lu T, Chen Y, Song Y, Wang S, et al. Oxygen-supplementing mesoporous polydopamine nanosponges with WS₂ QDs-embedded for CT/MSOT/MR imaging and thermoradiotherapy of hypoxic cancer. *Biomaterials.* 2019; 220: 119405.
40. Gunja N, Roberts D, McCoubrie D, Lambeth P, Jan A, Simes DC. Survival after massive hydroxychloroquine overdose. *Anaesth Intensive Care.* 2009; 37: 130-133.
41. Fang W, Tang S, Liu P, Fang X, Gong J, Zheng N. Pd nanosheet-covered hollow mesoporous silica nanoparticles as a platform for the chemo-photothermal treatment of cancer cells. *Small.* 2012; 8: 3816-3822.
42. Fan W, Shen B, Bu W, Chen F, He Q, Zhao K, et al. A smart upconversion-based mesoporous silica nanotheranostic system for synergetic chemo-/radio-/photodynamic therapy and simultaneous MR/UCL imaging. *Biomaterials.* 2014; 35: 8992-9002.
43. Liu Y, Ai K, Liu J, Deng M, He Y, Lu L. Dopamine-melanin colloidal nanospheres: an efficient near-infrared photothermal therapeutic agent for *in vivo* cancer therapy. *Adv Mater.* 2013; 25: 1353-1359.
44. Chen D, Li L, Tang F, Qi S. Facile and scalable synthesis of tailored silica "nanorattle" structures. *Adv Mater.* 2009; 21: 3804-3807.
45. Liu J, Bu J, Bu W, Zhang S, Pan L, Fan W, et al. Real-time *in vivo* quantitative monitoring of drug release by dual-mode magnetic resonance and upconverted luminescence imaging. *Angew Chem Int Ed Engl.* 2014; 53: 4551-4555.
46. Lin L, Cong Z, Cao J, Ke K, Peng Q, Gao J, et al. Multifunctional Fe₃O₄@Polydopamine core-shell nanocomposites for intracellular mRNA detection and imaging-guided photothermal therapy. *ACS Nano.* 2014; 8: 3876-3883.
47. Wang Y, Huang Q, He X, Chen H, Zou Y, Li Y, et al. Multifunctional melanin-like nanoparticles for bone-targeted chemo-photothermal therapy of malignant bone tumors and osteolysis. *Biomaterials.* 2018; 183: 10-19.
48. Wang X, Zhang J, Wang Y, Wang C, Xiao J, Zhang Q, et al. Multi-responsive photothermal-chemotherapy with drug-loaded melanin-like nanoparticles for synergetic tumor ablation. *Biomaterials.* 2016; 81: 114-124.
49. Wang X, Wang C, Wang X, Wang Y, Zhang Q, Chen Y. A polydopamine nanoparticle-knotted poly (ethylene glycol) hydrogel for on-demand drug delivery and chemo-photothermal therapy. *Chem Mater.* 2017; 29: 1370-1376.
50. Fu L, Qi C, Hu Y, Lin J, Huang P. Glucose oxidase-instructed multimodal synergistic cancer therapy. *Adv Mater.* 2019; 31: 1808325.
51. Zeng J, Liu W, Fan Y, He L, Li L. PrLZ increases prostate cancer docetaxel resistance by inhibiting LKB1/AMPK-mediated autophagy. *Theranostics.* 2018; 8: 109-123.
52. Lu Y, Zhang L, Li J, Su Y, Liu Y, Xu Y, et al. MnO nanocrystals: a platform for integration of MRI and genuine autophagy induction for chemotherapy. *Adv Funct Mater.* 2013; 23: 1534-1546.
53. Lin Y, Wang Y, Qiao S, An H, Wang J, Ma Y, et al. "In vivo self-assembled" nanopores for optimizing autophagy-mediated chemotherapy. *Biomaterials.* 2017; 141: 199-209.
54. Kuma A, Matsui M, Mizushima N. LC3, an autophagosome marker, can be incorporated into protein aggregates independent of autophagy: caution in the interpretation of LC3 localization. *Autophagy.* 2007; 3: 323-328.
55. Jiang P, Mizushima N. Autophagy and human diseases. *Cell Res.* 2014; 24: 69-79.